Research Square

Preprints are preliminary reports that have not undergone peer review.
They should not be considered conclusive, used to inform clinical practice,
or referenced by the media as validated information.

Ultra-High Discharge Voltage Plateau of 3.2 V Achieved in Li-CO2 Batteries Using Iron Polyphthalocyanine

Xiao Hu

xiaofei.hu@xjtu.edu.cn

Xi'an Jiaotong University

Ning Zhao

Xi'an Jiaotong University

Yi Zhang

University of Science and Technology of China

Limin Liu

Xi'an Jiaotong University

Han Zhang

Xi'an Jiaotong University

Xiao Wu

Xi'an Jiaotong University

Xuan Lu

Xi'an Jiaotong University

Han Yun

Xi'an Jiaotong University

Chang Zhang

Xi'an Jiaotong University

Yi Long

Xi'an Jiaotong University

Yang Gao

Xi'an Jiaotong University

Wen Su

Xi'an Jiaotong University

Rong Feng

Xi'an Jiaotong University

Zheng Meng

University of Science and Technology of China https://orcid.org/0000-0002-6775-3213

Shujiang Ding

Xi'an Jiaotong University https://orcid.org/0000-0002-5683-0973

Wen-feng Liu

Xi'an Jiaotong University

Qiang Wang

China Automotive Technology and Research Center Intelligent Technology (Tianjin) Co., Ltd.

Article

Keywords: Li-CO2 battery, High discharge voltage, Solid-state redox mediator, Wide temperature range

Posted Date: April 10th, 2026

DOI: https://doi.org/10.21203/rs.3.rs-9080697/v1

License: This work is licensed under a Creative Commons Attribution 4.0 International License.
Read Full License

Additional Declarations: There is **NO** Competing Interest.

Ultra-High Discharge Voltage Plateau of 3.2 V Achieved in Li-CO_2 Batteries Using Iron Polyphthalocyanine

Ning Zhao,[‡] Yi Zhang,[†] Li-Min Liu,[‡] Han-Qi Zhang,[‡] Xiao-Sha Wu,[‡] Xuan Lu,[‡] Han Yun,[‡] Changtong Zhang,[‡] Yini Long,[‡] Yang Gao,[‡] Wen-Long Su,[‡] Rong-Fen Feng,[‡] Zheng Meng*[,†], Shu-Jiang Ding,[‡,§] Wen-Feng Liu,[‡] Qiang Wang,[£] Xiao-Fei Hu*[,‡,§]

[‡]School of Chemistry, School of Electrical Engineering, Xi'an Jiaotong University, Xi'an, ShaanXi 710061, P. R. China

[†]State Key Laboratory of Precision and Intelligent Chemistry, School of Chemistry and Materials Science, University of Science and Technology of China, Hefei, Anhui 230026, P. R. China

[§]Engineering Research Center of Energy Storage Materials and Devices, Ministry of Education, Xi'an Jiaotong University. National Innovation Platform (Center) for Industry-Education Integration of Energy Storage Technology, Xi'an Jiaotong University, Xi'an, ShaanXi 710061, P. R. China

[£]China Automotive Technology and Research Center Intelligent Technology (Tianjin) Co., Ltd., Tianjin 300300, P. R. China

KEYWORDS: *Li-CO_2 battery, High discharge voltage, Solid-state redox mediator, Wide temperature range*

ABSTRACT: Rechargeable Li-CO_2 batteries offer great potential for greenhouse gas utilize and high-energy-density storage. However, their practical application is hindered by the formation of thermodynamically stable Li_2CO_3 product that is hard to decompose during charging. Highly crystalline and conductive reticular material iron-polyphthalocyanine (pFe^{II}Pc) as solid-phase redox mediator into Li-CO_2 batteries tailors the cathode reaction pathway, enabling stable $Li_2C_2O_4$ generation and an extraordinary discharge plateau of 3.2 V beyond the theoretical limit. Beyond delivering an ultrahigh discharge capacity of 28790 mAh g^{-1} and reversible cyclability over 1400 hours (1000 mAh g^{-1} cut-off capacity) at 100 mA g^{-1}, the Li-CO_2 batteries exhibit excellent temperature adaptability (-40 to 80°C). The Li-CO_2 pouch cells employing pFe^{II}Pc as solid-phase redox mediator achieve a high energy density of 678 Wh kg^{-1} based on total device mass and maintain reversible cycling for 251 hours. Our work pioneers a promising pathway toward practical high-efficiency Li-CO_2 batteries.

The excessive consumption on fossil fuels has resulted in an energy crisis and substantial CO_2 emissions, exerting profound adverse impacts on environmental integrity and sustainable economic development.[1-4] Consequently, developing innovative electrochemical energy storage device with dual energy-saving and emission-reduction capabilities has become an urgent imperative. Recently, the reversible lithium-carbon dioxide (Li-CO_2) batteries have emerged as promising candidates for next-generation energy storage systems owing to the superb theoretical energy density of 1876 Wh kg^{-1} and CO_2 utilization efficiency.[5-12] Furthermore, Li-CO_2 batteries exhibit unparalleled application potential in CO_2-rich environments, particularly for deep-sea missions and Mars exploration where atmospheric CO_2 concentrations exceed 95%.[13,14]

However, Li_2CO_3 pathway Li-CO_2 batteries typically exhibit limited discharge voltages of 2.0-2.5 V due to strong CO_2 bond interactions and sluggish reaction kinetics, significantly lower than the theoretical value of 2.8 V ($4Li^+ + 3CO_2 + 4e^- \rightarrow 2Li_2CO_3 + C$, E^0 = 2.80 V vs Li^+/Li).[15-22] Although the introduction of cobalt phthalocyanine (CoPc) has increased the discharge voltage of the Li-CO_2 battery via the Li_2CO_3-product pathway to 2.98 V, this additive suffers risks of contaminating lithium metal anodes and the high thermodynamic stability of Li_2CO_3 ($\Delta_fG^0(Li_2CO_3)$ = -1132.1 kJ mol^{-1}) results in a large overpotential, necessitating a charging voltage as high as 4.38 V for decomposition.[20,23-28] Notably, the theoretical decomposition voltage of side reaction in Li-CO_2 battery ($Li_2CO_3 - 2e^- \rightarrow 2Li^+ + CO_2 + 1/2\ {}^1O_2$, E^0 = 4.1 V versus Li/Li^+) is 4.1 V, indicating a high probability of parasitic reactions occurring.[29] The radical oxygen ($^1O_2$) produced by parasitic reactions may can aggressively degrade both electrodes and electrolyte, ultimately leading to abrupt death of Li-CO_2 batteries.[30]

In contrast to the Li_2CO_3 pathway (2.8 V), the $Li_2C_2O_4$-product route (3.01 V) exhibits superior theoretical discharge voltage and faster reaction kinetics in Li-CO_2 battery.[31,32] Also, the $Li_2C_2O_4$ exhibits both lower thermodynamic stability (Δ_fG^o = -286 kJ mol^{-1}) and diminished decomposition energy barriers (E_a = 0.75 eV) relative to Li_2CO_3 (E_a = 2.1 eV). As a result, Li-CO_2 batteries following the $Li_2C_2O_4$-product route deliver high energy efficiency and extended cycle life.[27,33,34] Attractively, recent studies have confirmed that heterogeneous catalysts (e.g., Mo-, and Ti-based materials) and homogeneous catalysts (e.g., Cu- and Ru-based complexes) can ensure the stable formation of $Li_2C_2O_4$ in Li-CO_2 battery through 2-electron reaction ($2Li^+ + 2CO_2 + 2e^- \leftrightarrow Li_2C_2O_4$, E^0 = 3.01 V versus Li/Li^+).[31-33,35,36] On the one hand, the use of heterogeneous catalysts enables stable formation of $Li_2C_2O_4$ in Li-CO_2 batteries, but the practical discharge voltage (2.8 V) of $Li_2C_2O_4$-product route Li-CO_2 battery remains below the theoretical value (3.01 V), and further improvements in cycle life are still required.[37] On the other hand, homogeneous catalysts (soluble redox mediators) indeed demonstrably elevate the discharge voltage plateau to approximately 3.0 V, yet the underlying mechanism for this high-voltage platform remains unclear. More importantly, homogeneous catalysts inherently suffer from inevitable critical limitations, including poor solubility, sluggish kinetics, severe

corrosion of lithium anodes, and pronounced self-decomposition, which severely restrict the practical application of homogeneous catalysts Li-CO_2 batteries.[36,38,39] Accordingly, the rational design of high-efficiency solid-state redox mediators represents a promising strategy for elevating the discharge voltage plateau (to >3.01 V) in $Li_2C_2O_4$-product route Li-CO_2 battery.

Herein, a highly crystalline and conductive reticular material pFe^{II}Pc was introduced as a solid-state redox mediator for Li-CO_2 batteries.[40] As shown in Scheme 1a, employing pFe^{I}Pc as solid-state redox mediators in Li-CO_2 batteries not only achieves stable generation of $Li_2C_2O_4$ but also boosts the discharge voltage to 3.2 V, exceeding theoretical limit. The solid-state redox mediators pFe^{II}Pc features a conductive and stable network structure, along with precisely distributed single-active sites and multi-active centers. Owing to pFe^{II}Pc ultrahigh electron affinity and excellent stabilizing effect on $Li_2C_2O_4$, pFe^{II}Pc preferentially accepts electrons instead of CO_2, then transfers the captured electrons to CO_2 to form CO_2^- (activation), while simultaneously adsorbing Li^+ ions (Scheme 1b-1c). Ultimately, the monomers undergo coupled catalysis to form the final product $Li_2C_2O_4$, which is stabilized by pFe^{II}Pc. Therefore, the Li-CO_2 batteries with pFe^{II}Pc as solid-state redox mediator exhibits ultrahigh discharge voltage plateau of 3.2 V, an exceptional discharge capacity of 28790 mAh g^{-1} with a reversible charge capacity of 21698 mAh·g^{-1}, a low voltage gap of 0.58 V, a long cycling life exceeding 1480 hours, and ultra-wide temperature range operation (-40~80 °C). As a proof of concept, the Li-CO_2 pouch cells achieve an energy density of 678 Wh kg^{-1} based on the total device mass and demonstrate stable cycling performance. This work is expected to accelerate the practical application of Li-CO_2 batteries.

Results and discussion

Electrochemical performance of Li-CO_2 battery catalyzed by pFe^{I}Pc

Highly crystalline and conductive pFe^{II}Pc has been successfully synthesized through the annulation of tetracyanobenzene in the presence of transition metals (Figure S1). A typical three-electrode cell with controlled atmosphere was employed to investigate the catalytic activity of pFe^{II}Pc cathode toward the CO_2 reduction reaction (CO_2RR). As shown in Figure 1a and Figure S2, under Ar atmosphere the solid-phase redox mediator pFe^{II}Pc exhibits a pair of redox peaks at 3.23V (E_{d1}) and 3.45V (E_{c1}), which suggests the possible occurrence of a reversible redox reaction between Fe^{II}and Fe^{I} in the solid-state redox mediator pFe^{II}Pc. Similarly, a reduction peak observed at the same position (3.23 V, E_{d2}) on the CV curve indicates that the same reduction process occurs in the solid-phase redox mediator pFe^{II}Pc under CO_2 atmosphere. This can be ascribed to the reduction reaction of pFe^{II}Pc and pFe^{I}Pc, as traced in Eq.1. Additionally, compared to the oxidation peak observed in Ar, the oxidation peak in CO_2 appears at 3.75 V (E_{c2}), which is attributed to the decomposition of the discharge product $Li_2C_2O_4$, facilitated by the electron-transfer cascade from pFe^{I}Pc to CO_2 during $Li_2C_2O_4$ formation. Both in-situ online Gas Chromatography-Mass Spectrometry and experimental results demonstrate that pFe^{II}Pc, after gaining electrons and being reduced to pFe^{I}Pc, can promote the CO_2 reduction reaction (Figures S3-5). As shown in Figure S6, the Ultraviolet-Visible Spectroscopy (UV-Vis) spectroscopy shows no notable shift in the spectral features after discharge in CO_2, while a blueshift in the characteristic peaks is observed after discharge in Ar, which aligns with the expected reduction of pFe^{II}Pc to pFe^{I}Pc.[41] By comparing the above results, it can be concluded that in the presence of solid-phase redox mediator pFe^{II}Pc, the reaction pathway of the Li-CO_2 battery is altered by the transfer of electrons from pFe^{I}Pc to CO_2.

$$pFe^{II}Pc + e^- \leftrightarrow pFe^{I}Pc \quad (1)$$

Li-CO_2 batteries were assembled with and without pFe^{II}Pc to further investigate the electrochemical performance of the solid-state redox mediator pFe^{II}Pc. The full charge-discharge process was conducted within a voltage range of 2.0–4.5 V at 100 mA g^{-1}, as provided in Figure 1b. Remarkably, Figure 1b shows that the solid pFe^{II}Pc cathode in CO_2 atmosphere exhibits outstanding stability, with an initial discharge capacity as high as 28790 mAh g^{-1} and reversible capacity of 26338 mAh g^{-1}. Also, the solid pFe^{II}Pc cathode shows severely limited performance in Ar atmosphere, with discharge and charge capacities of only 1560 mAh g^{-1} and 1364 mAh g^{-1}, respectively. In the control group, the Li-CO_2 battery without pFe^{II}Pc demonstrates limited performance under CO_2, achieving merely 9468 mAh g^{-1} discharge capacity and 7531 mAh g^{-1} recharge capacity. As illustrated in Figure 1c, the Li-CO_2 battery containing pFe^{II}Pc demonstrates not only a high discharge voltage plateau of 3.2 V (considerably exceeding the theoretical discharge voltage of 3.01 V) but also achieves a reduced charge voltage of 3.7 V compared to its pFe^{II}Pc-free counterpart. More importantly, it exhibits a significantly lower overpotential of merely 0.58 V, representing just one-third of that observed in the control group (1.74 V). Meanwhile, rate capability is a critical parameter for evaluating reaction kinetics, which was assessed at multiple current densities under a fixed cut-off capacity of 1000 mAh g^{-1}. As shown in Figures 1d-1e, with current density increased progressively from 100 to 1000 mA g^{-1}, the Li-CO_2 battery with pFe^{II}Pc demonstrated a controlled voltage gap expansion (0.58→1.3 V), markedly lower than the pronounced polarization increase (1.66→2.06 V) observed in pFe^{II}Pc-free counterpart cell. Notably, upon recovering the current density to 100 mA g^{-1}, the potential gap of the Li-CO_2 battery with pFe^{II}Pc returned to 0.73 V. Remarkably, the Li-CO_2 battery with pFe^{II}Pc maintains a discharge voltage plateau exceeding 3.01 V even at 600 mA g^{-1}, with a high median discharge voltage of 2.8 V persisting at ultrahigh 1000 mA g^{-1}. To systematically evaluate the cycling stability, Li-CO_2 batteries with and without pFe^{II}Pc were subjected to extended cycling tests at varying current densities with cut-off capacity of 1000 mAh g^{-1}. Figure 1f demonstrates the stable cycling stability of the pFe^{II}Pc cathode, maintaining stable operation for 40 cycles with a 3.01 V discharge termination potential and < 4.1 V charge voltage plateau, and energy efficiency stays above 75%. Moreover, the Li-CO_2 battery with pFe^{II}Pc also displays prolonged cycling stability, maintaining continuous operation for 1482 hours at 100 mA g^{-1}

(Figure 1g, Figure S7). This is due to the extremely low solubility of pFe^{II}Pc in the electrolyte, as well as the fact that during cycling in the Li-CO_2 battery, the crystal structure of pFe^{II}Pc remains intact, without significant evolution or degradation, and the valence state of its catalytic active sites remains unchanged (Figure S8-10). To evaluate high-rate cycling stability, Li-CO_2 batteries with pFe^{II}Pc were tested at elevated current densities under a cut-off capacity of 1000 mAh g^{-1}. The cells exhibited sustained operation for 191 and 139 hours at 600 and 1000 mA g^{-1} (Figure S11). This special electrochemical performance stems directly from pFe^{II}Pc superior conductive and catalytic activity, which mitigates polarization and enhances reaction kinetics.

The Li-CO_2 battery with pFe^{II}Pc maintains excellent performance across an ultra-wide operating temperature range, beyond room temperature. The electrochemical performance of the Li-CO_2 battery with pFe^{II}Pc under a cut-off capacity of 500 mAh g^{-1} was evaluated at temperatures ranging from -40 °C to 80 °C (-40 °C, -30 °C, -20 °C, 0 °C, 20 °C, 40 °C, 60 °C, and 80 °C), as presented in Figure 1h. Despite the voltage gap is slightly larger at -30 °C and -20 °C, the pFe^{II}Pc-based Li–CO_2 battery retains a stable 2.9 V discharge voltage plateau and consistently operates above 3.01 V from 0 °C to 80 °C (Figure S12). The Li-CO_2 battery with pFe^{II}Pc demonstrates excellent electrochemical performance over a wide temperature range. However, the discharge plateau inevitably decreases as the temperature drops, which is attributed to the temperature dependence of pFe^{II}Pc conductivity, as its electrical conductivity decreases with lowering temperature (Figures S13-14). Intriguingly, the battery maintains normal operation even at -40°C, which is attributed to the extraordinary catalytic properties of pFe^{II}Pc across an ultra-wide operating temperature range. At the same time, the porous structure in the separator also helps to lower the freezing point of the electrolyte to some extent, further enhancing the performance of Li-CO_2 battery at low temperatures (Figure S15). In-situ temperature-dependent Raman spectroscopy further confirms this observation (Figures 2a-2b, Figure S16), the pFe^{II}Pc maintaining structural integrity over -60 to 80°C, confirming superior wide-temperature stability. In addition, the Li-CO_2 battery using pFe^{II}Pc as the solid-state redox mediator exhibits stable cycling performance at -20 °C and -80 °C (Figure S17).

Product characterization of Li-CO_2 batteries catalyzed by pFe^{II}Pc

To investigate the discharge products and the reversibility of the Li-CO_2 battery, a series of in-situ and ex situ characterizations were conducted during the charge–discharge process. As evident in Figure 2c, products deposited on the carbon fibers were clearly visible after discharging but disappeared following complete recharge. Ex situ XPS and TOF-SIMS were employed to further identify the species of the discharge products. The XPS spectra of C 1s and Li 1s were comparatively analyzed in the pristine state, after discharge, and after recharge (Figure 2d and Figure S18). The XPS spectra of C 1s from the discharged electrode clearly exhibits characteristic peaks at 288.90 eV (O-C=O) which unambiguously confirm the formation of $Li_2C_2O_4$ as the discharge product.

More importantly, two prominent signals observed after discharge at m/z 101.98 and 88 in Figure 2e and Figure S19 exhibits exact correspondence with the $Li_2C_2O_4$ and disappears after charging, providing direct evidence for $Li_2C_2O_4$ formation during discharge. Additionally, the TOF-SIMS results show that no prominent signals appear at m/z of 23 and 60, confirming that lithium carbonate is absent in the products (Figure S19). The ex-situ XRD and Raman analyses of the deep discharge products also confirm that $Li_2C_2O_4$ is the final discharge product (Figure S20). The dynamic evolution of discharge/charge processes was monitored in real-time using a specially designed in-situ XRD and Raman electrochemical cells (Figure 2f and Figure S21). Figure 2g presents the galvanostatic charge-discharge profiles of the in-situ Li-CO_2 XRD battery employing pFe^{II}Pc cathode, demonstrating a reversible capacity of 1600 mAh g^{-1} at a current density of 200 mA g^{-1}. The XRD diffraction peak intensities of $Li_2C_2O_4$ at $2\theta = 36.44°$ and 40.64° progressively intensify with increasing discharge depth and systematically diminish during the charging process, exhibiting a reversible evolution pattern. Consistent with the in-situ XRD findings, complementary in-situ Raman spectroscopy corroborated these observations. As Figure 2h documents, the Raman peak intensities associated with $Li_2C_2O_4$ at 865 cm^{-1} (C-C) and 1486 cm^{-1} (C=O) exhibited a discharge-depth-dependent enhancement. These spectral features exhibited progressive attenuation during charging and ultimately disappeared upon reaching full state of charge. The pFe^{II}Pc as solid-phase catalyst in Li-CO_2 battery that not only directs the discharge product to $Li_2C_2O_4$ but also promotes reversible CO_2 redox.

Mechanistic analysis of the ultra-high discharge plateau

The quantitative DEMS was employed to analyze the electrons transferred on the pFe^{II}Pc surface as well as the consumption and evolution of CO_2. The dual-gas-path in-situ DEMS testing during the charge-discharge process is illustrated in the Figure 3a and Figure S22. The transferred charge-to-CO_2 consumption ratio (e^-/CO_2) for the reaction $2Li^+ + 2CO_2 + 2e^- \rightarrow Li_2C_2O_4$ is determined to be 1 during the charge-discharge process. The near-unity e^-/CO_2 ratio (0.97) observed during discharge suggests highly efficient CO_2 utilization and effective $Li_2C_2O_4$ formation on the pFe^{II}Pc electrode (Figure 3b). Moreover, analyses of the evolved gas species and the CO_2 evolution mechanism were conducted during the charge process. As evidenced in Figure 3c, the recharge process exclusively produced CO_2, with no detectable O_2 and CO generation, demonstrating the reversible nature of the CO_2 evolution (Figure S23). DEMS measurements show a 1.04 e^-/CO_2 ratio during charging, consistent with the theoretical value of 1 e^-/CO_2 predicted by the reversible CO_2 evolution reaction ($Li_2C_2O_4 \rightarrow 2Li^+ + 2CO_2 + 2e^-$). Therefore, these findings confirm that the Li-CO_2 battery employing pFe^{II}Pc as solid-phase redox mediator undergoes a 2-electron transfer process, with $Li_2C_2O_4$ as the main discharge product.

To elucidate the formation mechanism of $Li_2C_2O_4$ and ultra-high discharge platform mechanism on solid pFe^{II}Pc cathode, the

cathode surface composition at various electrochemical stages was systematically analyzed by ex situ XPS and DFT. First, XPS analysis reveals that the Fe 2p spectrum of the pristine pFe^{II}Pc cathode under Ar atmosphere (Figure 3d, top) exhibits a single characteristic peak at ~707.2 eV, confirming the exclusive presence of Fe^{II} in the pristine pFe^{II}Pc cathode. As the discharge progresses (Figure 3d, middle), a new peak emerges at ~705.4 eV under Ar, attributed to the increased Fe^{I} state. Concurrently, the Fe^{I} signal diminishes substantially, indicating near-complete reduction to Fe^{I}. Strikingly, the Fe^{I} valence state shows no change after CO_2-assisted discharge, in sharp contrast to the Ar case (Figure 3d, bottom). This provides direct evidence for the rapid electron shuttle mechanism: reduced Fe^{I} promptly donates its electrons to CO_2 and is thereby oxidized back to Fe^{II}. This conclusion is fully consistent with the CV results, corroborating the proposed reaction mechanism and ultra-high discharge platform mechanism. Subsequently, the formation of $Li_2C_2O_4$ in CO_2 atmosphere is confirmed by the appearance of two characteristic peaks: The C 1s (O-C=O) at 288.90 eV and the Li 1s at 55.34 eV (Figures 3e-f). This phenomenon was not observed in the Ar atmosphere, confirming the CO_2-dependent nature of $Li_2C_2O_4$ formation and pFe^{II}Pc solely as a redox mediator. An unexpected Li signal appeared on the electrode after discharge in AR, which is attributed to the precipitation of lithium salts in the electrolyte and the contribution of Li from the Cathode Electrolyte Interphase (CEI). Furthermore, DFT calculations reveal that pFe^{II}Pc exhibits an electron affinity of 4.91 eV (Figure S24). This thermodynamic preference ensures pFe^{II}Pc as the preferential electron acceptor: pFe^{II}Pc is preferentially reduced (pFe^{II}Pc + e^- → pFe^{I}Pc) and subsequently mediates electron donation to CO_2 for the ensuing electrochemical reactions.

Reaction pathway for $Li_2C_2O_4$ formation from CO_2 catalyzed by pFe^{II}Pc

The DFT calculation was employed to systematically investigate the stability of $Li_2C_2O_4$ on the pFe^{II}Pc surface. Figure 4a and Figures S25-27 presents the DFT-optimized adsorption configurations and corresponding adsorption energies of $Li_2C_2O_4$ on $C_{32}H_{16}N_8Fe$, $C_{58}H_{26}N_{16}Fe_2$, and CNT, respectively. The calculated adsorption energy of $Li_2C_2O_4$ on $C_{32}H_{16}N_8Fe$ (-1.21 eV) is markedly higher than those on $C_{58}H_{26}N_{16}Fe_2$ (-0.68 eV) and CNT (-0.61 eV), indicating preferential stabilization of $Li_2C_2O_4$ as discharge products on the $C_{32}H_{16}N_8Fe$ surface during the discharge process. To clarify the reaction mechanism of $Li_2C_2O_4$ on redox mediator surface during discharge, two distinct reaction pathways employing monomer $C_{32}H_{16}N_8Fe$ and $C_{58}H_{26}N_{16}Fe_2$ as catalytic units were computationally investigated. Figure 4b presents the free energy profiles for the most probable $2e^-/2CO_2$ nucleation pathways of $Li_2C_2O_4$ formation on surfaces $C_{32}H_{16}N_8Fe$ and $C_{58}H_{26}N_{16}Fe_2$. The two dominant reaction pathways proceed as follows:

Path Ⅰ: * + (Li^+ + e^-) →*Li^+ + CO_2 (g) → *$LiCO_2$ + (Li^+ + e^-) → *Li_2CO_2 + CO_2 (g) →*$Li_2C_2O_4$ →* + $Li_2C_2O_4$

Path Ⅱ: $^{\#}$ + 2(Li^+ + e^-) →$^{\#}$2Li^+ + CO_2 (g) → $^{\#}$$LiCO_2Li^+$ + CO_2 (g) → $^{\#}$2($LiCO_2$) →$^{\#}$$Li_2C_2O_4$ →$^{\#}$ + $Li_2C_2O_4$

In both pathways, all Li^+-involving steps with electron transfer exhibit exothermic downhill profiles in the free energy diagrams, confirming their spontaneous nature. However, both the CO_2 adsorption on *Li_2CO_2 to form *$Li_2C_2O_4$ in Pathway I and $^{\#}$2($LiCO_2$) to form $^{\#}$$Li_2C_2O_4$ in Pathway II exhibit endothermic characteristics. These endothermic uphill steps serve as the rate-determining steps for $Li_2C_2O_4$ formation in both Pathway I and Pathway II. The activation energy barrier for the rate-determining step in Pathway I (0.49 eV) is substantially lower than those in Pathway II (0.71 eV). The overall Gibbs free energy change (ΔG) for $Li_2C_2O_4$ decomposition in Pathway I (2.57 eV) is considerably more negative than that in Pathway II (4.68 eV). These findings unambiguously demonstrate that the steady $Li_2C_2O_4$ electrochemistry via the $2e^-/2CO_2$ reaction preferentially follows Pathway I in pFe^{II}Pc-based Li-CO_2 batteries (Figure 4c). Based on the optimal reaction pathway determined through dynamic simulations via $Li_2C_2O_4$ formation, we have captured the dynamic evolution of characteristic vibrational peaks of Li-O and $C_2O_4^{2-}$ intermediates during discharge in in-situ Raman spectroscopy (Figure 4d). The $Li_2C_2O_4$ can serve as the final discharge product in the Li-CO_2 battery due to its stronger adsorption energy with pFe^{II}Pc. Additionally, projected Density of States (PDOS) analysis shows that the interaction between $Li_2C_2O_4$ and pFe^{II}Pc primarily occurs near the Fermi level (-2 to 0 eV). In comparison to Li_2CO_3 (−4 eV to 0 eV), the O-p orbital distribution in *$Li_2C_2O_4$ is narrower, indicating that the p-electrons of the oxygen atoms in the *$Li_2C_2O_4$ are more concentrated near the Fermi level, resulting in a lower and more stable energy state (Figure 4e and Figures S28-29).

Proof-of-concept Li-CO_2 pouch cells were demonstrated using pFe^{I}Pc as solid-phase redox mediator cathodes paired with LITFSI/TEGDME electrolytes. As shown in Figure 4f, the Li-CO_2 pouch cell (5.5 cm × 4 cm, 2.19 g) exhibits a discharge voltage plateau 3.1 V with a high discharge capacity of 479 mAh at room temperature under 100 mA g^{-1}, delivering an impressive energy density of 678 Wh kg^{-1} based on the total pouch cell mass. In addition, the Li-CO_2 pouch cell employing pFe^{II}Pc as solid-phase redox mediator cathodes with a cut-off capacity of 500 mAh g^{-1} at 100 mA g^{-1} maintains a discharge voltage plateau above 3.01 V for 19 reversible cycles, with a total cycle duration of up to 251 hours (Figure 4g). As displayed in Figure 4h, the pouch cell successfully powered light-emitting diodes (LEDs) under simulated Martian conditions (95% CO_2), demonstrating that the pFe^{II}Pc-based Li-CO_2 battery technology holds significant potential for practical applications.

In summary, we proposed a novel strategy that utilizes pFe^{I}Pc with ultrahigh electron affinity as solid-state redox mediator to achieve the $Li_2C_2O_4$-product pathway while elevating the discharge voltage plateau of Li-CO_2 batteries to 3.2 V, enabling long-term stable reversible cycling based on the $Li_2C_2O_4$ pathway. The reaction mechanism of Li-CO_2 batteries using pFe^{I}Pc as the cathode material is collectively elucidated by electrochemical studies, in-situ spectroscopic characterization, and DFT calculation. During discharge, pFe^{I}Pc preferentially accepts electrons from the anode instead of CO_2, being reduced

to $pFe^{I}Pc$. Subsequently, $pFe^{I}Pc$ rapidly transfers these electrons to CO_2 (thereby being oxidized back to $pFe^{I}Pc$), and ultimately the reduced CO_2 reacts with Li^+ to form $Li_2C_2O_4$. Notably, $pFe^{I}Pc$ exhibits strong adsorption energy toward $Li_2C_2O_4$, thereby stabilizing the $Li_2C_2O_4$ product. Since the reduction potential of $pFe^{I}Pc$ accepting electrons to form $pFe^{I}Pc$ exceeds 3.01 V, this process results in the battery demonstrating a discharge voltage plateau higher than its theoretical value. As proof-of-concept reliability verification candidate, the $pFe^{I}Pc$ demonstrated exceptional catalytic kinetics in Li-CO_2 battery, delivering an ultrahigh discharge capacity of 28790 mAh g^{-1} and reversible cyclability exceeding 1400 hours at 100 mA g^{-1}. With the introduction of $pFe^{I}Pc$ not only enables the $Li_2C_2O_4$ pathway in Li-CO_2 batteries but also achieves a discharge voltage plateau of 3.2 V. The designed Li-CO_2 battery system enables superb wide-temperature operability (-40 to 80°C). Ultimately, our engineered pouch cell achieves an energy density of 678 Wh kg^{-1} while maintaining stable cycling performance over 251 hours. This research provides a universally effective strategy for the practical application of Li-CO_2 batteries.

Methods

Materials

Super P, Poly (vinylidene fluoride-co-hexafluoropropylene) (PVDF-HFP, average Mn of ~130000), N-methyl-2-pyrrolidinone (NMP, 99.5 %) were purchased from Sigma-Aldrich. 1.0 M Lithium bis (trifluoromethanesulphonyl) imide/Tetraglyme (LiTFSI/TEGDME) electrolyte, was purchased from Fosai. Carboxylated multi-walled carbon nanotubes (CNT, >95%) was purchased from MREDA. 1, 2, 4, 5-tetracyanobenzene was purchased from Sigma-Aldrich. Iron powder (Fe, 99.9%, 50 nm, 7439-89-6) was purchased from Macklin.

Synthesis of $pFe^{II}Pc$

1, 2, 4, 5-tetracyanobenzene (50 mg, 0.28 mmol) was mixed with iron powder (31.5 mg, 0.56 mmol). The mixture was thoroughly ground and transferred into a Pyrex tube measuring o.d. × i.d. = 10 × 8 mm^2. The Pyrex tube was then evacuated and flame-sealed with the total length kept at ca. 5.0 cm. The glass tube was heated to 400 °C at 5 °C /min and kept for 4 h in a tube furnace under vacuum conditions. After cooling to room temperature, the product was washed several times with ethanol, iron chloride solution, and H_2O and then dried at 60 °C in a vacuum oven to afford a purple-black powder.

Li-CO_2 batteries assembly

In the preparation of porous cathode. Experimental group: 45 wt % Super P, 45 wt % $pFe^{II}Pc$ and 10 wt % PVDF were mixed in appropriate NMP. Control group: 45 wt % Super P, 45 wt % CNT and 10 wt % PVDF were mixed in appropriate NMP. The resulting slurry was then pasted on a carbon paper and loading mass of active materials on the carbon cloth was ~0.2 mg. 1.0 M LiTFSI/TEGDME electrolyte was used as the electrolyte. CR2032 coin batteries with holes for CO_2 permeation were assembled with the as-prepared cathodes, glass fiber separator, Li metal anode and 80 μL as-prepared electrolyte in a glovebox filled with ultrapure Argon. The assembled Li−CO_2 batteries were then placed in a sealed glass bottle filled with CO_2 and rested for 8 hours before testing with a Land battery tester at different temperature.

Characterizations and Electrochemical Measurements

The CV testing was conducted in a specialized three-electrode cell, with a scan rate of 10 mV/s and a voltage testing range of 2.0-4.0 V during the process. The morphologies and structures of discharge product were characterized by using SEM (Gemini SEM 500) and. X-ray diffraction (XRD) patterns were collected with a Bruker D8 ADVANC diffractometer using Cu Kα radiation at a 2° min^{-1} scan rate was used to acquire the in-situ XRD results. The Renishaw Raman spectrometer (InVia Qontor) with a 532 nm wavelength incident laser was applied to obtain the in-situ Raman spectra. X-ray Photoelectron Spectroscopy (XPS) measurements were performed on a Thermo Scientific K-Alpha instrument. The electrochemical mass spectrometry (DEMS) measurements were performed by a quadrupole mass spectrometer (PrismaPro) with a turbomolecular pump (Pfeiffer Vacuum). The mechanism analysis was obtained through Time of Flight secondary Ion Mass Spectrometer (TOF-SIMS, M6). Land cycler (Wuhan Land Electronic Co. Ltd.) was employed for galvanostatic charge-discharge tests of Li−CO_2 batteries. The calculation of specific capacities and current densities were all based on the mass loading of pFePc and CNT. The electrochemical stability of pFePc and CNT were performed by cyclic voltammetry (CV) conducted on an electrochemical workstation (CHI 660E) at the sweep rate of 1.0 mV s^{-1}.

Computational methods

Electronic calculations were performed to determine the adsorption energy and free energy profiles using spin-polarized density functional theory (DFT) in the Vienna Ab initio Simulation Package (VASP) with a plane-wave basis set and the Vienna ab initio simulation package (VASP) method.[42,43] The exchange-correlation potential was treated by using a generalized gradient approximation (GGA) with the Perdew-Burke-Ernzerhof (PBE) parametrization.[44] A vacuum region of about 15 Å was applied to avoid the interaction between adjacent images. The energy cutoff was set to be 450 eV. A Monkhorst−Pack k-point mesh of 1× 1× 1 was used for structural Optimizations. The structures were fully relaxed until the maximum force on each atom was less than 0.02 eV/Å, and the energy convergent standard was 10^{-5} eV.

Equation 1 is used to calculate the adsorption energy:

$$E_{ads} = E_{total} - E_{slab} - E_{adsorbate} \quad (1)$$

where E_{total} is the total energy of the adsorbate-substrate system, E_{slab} is the energy of the clean substrate material, and $E_{adsorbate}$ is the energy of the isolated adsorbate.

Equation 2 is used to calculate the free energy for each adsorbed and gas-phase species. The Gibbs free energy G and change (ΔG) of each elementary step can be simplified to[45]

$$\Delta G = \Delta E + \Delta E_{ZPE} - T\Delta S + \Delta G_{pH} \quad (2)$$

In equation 2, T denotes the system temperature (298.15 K), while ΔE, ΔE_{ZPE}, and ΔS represent the total electronic energy, zero-point energy, and entropy change of the reaction, respectively, as obtained from density functional theory (DFT) calculations. ΔG_{pH} is the correction of pH value for Gibbs free energy and pH is equal to zero in this work. The two dominant reaction pathways proceed as follows:

Pathway Ⅰ:

i: $C_{32}H_{16}N_8Fe^{Ⅱ} + Li^+ + e^- \rightarrow C_{32}H_{16}N_8Fe^{Ⅰ}Li^+$

ii: $C_{32}H_{16}N_8Fe^{Ⅰ}Li^+ + CO_2(g) \rightarrow C_{32}H_{16}N_8Fe^{Ⅱ}LiCO_2$

iii: $C_{32}H_{16}N_8Fe^{Ⅱ}LiCO_2 + Li^+ + e^- \rightarrow C_{32}H_{16}N_8\ Fe^{Ⅰ}Li_2CO_2$

iv: $C_{32}H_{16}N_8Fe^{Ⅰ}Li_2CO_2 + CO_2(g) \rightarrow C_{32}H_{16}N_8Fe^{Ⅱ}Li_2C_2O_4$

v: $C_{32}H_{16}N_8Fe^{Ⅱ}Li_2C_2O_4 \rightarrow C_{32}H_{16}N_8Fe^{Ⅱ} + Li_2C_2O_4$

Pathway Ⅱ:

i: $C_{58}H_{26}N_{16}Fe_2^{Ⅱ} + 2Li^+ + 2e^- \rightarrow C_{58}H_{26}N_{16}Fe_2^{Ⅰ}2Li^+$

ii: $C_{58}H_{26}N_{16}Fe_2^{Ⅰ}2Li^+ + CO_2(g) \rightarrow C_{58}H_{26}N_{16}Fe^{Ⅰ}Fe^{Ⅱ}LiCO_2Li^+$

iii: $C_{58}H_{26}N_{16}Fe^{Ⅰ}Fe^{Ⅱ}LiCO_2Li^+ + CO_2(g) \rightarrow C_{58}H_{26}N_{16}Fe_2^{Ⅱ}LiCO_2CO_2Li$

iv: $C_{58}H_{26}N_{16}Fe_2^{Ⅱ}LiCO_2CO_2Li \rightarrow C_{58}H_{26}N_{16}Fe_2^{Ⅱ}Li_2C_2O_4$

v: $C_{58}H_{26}N_{16}Fe_2^{Ⅱ}Li_2C_2O_4 \rightarrow C_{58}H_{26}N_{16}Fe_2^{Ⅱ} + Li_2C_2O_4$

Data availability

The data generated in this study are provided in the paper and Supplementary Information. Additional relevant data are available from the corresponding author on request.

References

1. Zhang, F. et al. Boosting a practical lithium carbon dioxide battery through a decoupled electrolyte. *Nat. Commun.* **16**, 9305 (2025).
2. Zhang, J. et al. High-Energy-Density Li-CO_2 Battery at Elevated Temperatures: Advances with Fluorine-Substituted Graphdiyne and Ionic Liquid. *Angew. Chem. Int. Ed.* **64**, e202420892 (2025).
3. Hu, S. et al. Electronic Localization Modulation of the Cyano-Bridged $Cu_3[Co(CN)_6]_2$ Catalyst With Heterometallic Active Sites for High-Performance Li-CO_2 Batteries. *Adv. Energy Mater.* **15**, 2501001 (2025).
4. Chen, B. et al. Designing Electrophilic and Nucleophilic Dual Centers in the ReS_2 Plane toward Efficient Bifunctional Catalysts for Li-CO_2 Batteries. *J. Am. Chem. Soc.* **144**, 3106–3116 (2022).
5. Liu, Y. et al. Deciphering the contributing motifs of reconstructed cobalt (II) sulfides catalysts in Li-CO_2 batteries. *Nat. Commun.* **15**, 2167 (2024).
6. Lin, J. et al. Boosting Energy Efficiency and Stability of Li–CO_2 Batteries via Synergy between Ru Atom Clusters and Single-Atom Ru–N_4 sites in the Electrocatalyst Cathode. *Adv. Mater.* **34**, 2200559 (2022).
7. Chen, J. et al. Recent progress of transition metal-based catalysts as cathodes in O_2/H_2O-involved and pure Li–CO_2 batteries. *Energy Environ. Sci.* **16**, 792–829 (2023).
8. Cheng, Z. et al. Lewis Acidity-Enhanced Metal-Organic Frameworks as High-Efficiency Cathode Catalysts for Advanced Li-CO_2 Batteries. *Adv. Funct. Mater.* **35**, 2504330 (2025).
9. Chen, H. et al. Ferrocene-Based Nickel Metal–Organic Framework Nanosheets as Efficient, Long-Cycle Cathode Catalyst for Li-CO_2 Battery. *Adv. Funct. Mater.* **35**, 2412387 (2025).
10. Da, X. et al. CO_2-Assisted Induced Self-Assembled Aramid Nanofiber Aerogel Composite Solid Polymer Electrolyte for All-Solid-State Lithium-Metal Batteries. *Adv. Energy Mater.* **14**, 2303527 (2024).
11. Han, J. et al. Bioinspired iron porphyrins with appended poly-pyridine/amine units for boosted electrocatalytic CO_2 reduction reaction. *eScience* **2**, 623–631 (2022).
12. Wang, Y. et al. Surface Superlattice-Induced Spatial Confinement Enables High Voltage and Long Cycle Life in Li–CO_2 Batteries. *J. Am. Chem. Soc.* (2026).
13. Zhou, J. et al. A Quasi-Solid-State Flexible Fiber-Shaped Li–CO_2 Battery with Low Overpotential and High Energy Efficiency. *Adv. Mater.* **31**, 1804439 (2019).
14. Zhang, Z. et al. Exploiting Synergistic Effect by Integrating Ruthenium–Copper Nanoparticles Highly Co-Dispersed on Graphene as Efficient Air Cathodes for Li–CO_2 Batteries. *Adv. Energy Mater.* **9**, 1802805 (2019).
15. Hu, K. et al. Photoassisted Li–CO_2 Batteries with Ultrahigh Energy Efficiency and Cycle Stability by a Redox Mediator. *ACS Nano* **19**, 7707–7717 (2025).
16. Yang, M. et al. Deep Eutectic Solvent Additive Induced Inorganic SEI and an Organic Buffer Layer Synergistic Protected Li Anode for Durable Li-CO_2 Batteries. *Adv. Energy Mater.* **15**, 2405628 (2025).
17. Zou, J. et al. Revisiting the Role of Discharge Products in Li–CO_2 Batteries. *Adv. Mater.* **35**, 2210671 (2023).
18. Pan, Q. et al. Approaching Splendid Catalysts for Li–CO_2 Battery from the Theory to Practical Designing: A Review. *Adv. Mater.* **36**, 2406905 (2024).
19. Zhang, K. et al. Boosting Cycling Stability and Rate Capability of Li–CO_2 Batteries via Synergistic Photoelectric Effect and Plasmonic Interaction. *Angew. Chem. Int. Ed.* **61**, e202201718 (2022).
20. Zhao, N. et al. Elevating Discharge Voltage of Li_2CO_3-Routine Li−CO_2 Battery over 2.9 V at an Ultra-Wide Temperature Window. *Angew. Chem. Int. Ed.* **63**, e202407303 (2024).
21. Jian, T., Ma, W., Xu, C., Liu, H. & Wang, J. Intermetallic-driven highly reversible electrocatalysis in Li–CO_2 battery over nanoporous Ni_3Al/Ni heterostructure. *eScience* **3**, 100114 (2023).
22. Gao, F. et al. Unveiling the Solvation Chemistry and Surface Effects on CO_2 Reduction Reaction Pathways in Nonaqueous Li–CO_2 Batteries. *J. Am. Chem. Soc.* **147**, 19859–19867 (2025).
23. Wang, S. et al. An ultralow-charge-overpotential and long-cycle-life solid-state Li-CO_2 battery enabled by plasmon-enhanced solar photothermal catalysis. *Nano Energy* **100**, 107521 (2022).
24. Wang, F. et al. Metal–CO_2 Electrochemistry: From CO_2 Recycling to Energy Storage. *Adv. Energy Mater.* **11**, 2100667 (2021).
25. Liu, Y. et al. Toward an Understanding of the Reversible Li-CO_2 Batteries over Metal–N_4-Functionalized Graphene Electrocatalysts. *ACS Nano* **16**, 1523–1532 (2022).
26. Wang, M. et al. Atomically Dispersed Manganese on Carbon Substrate for Aqueous and Aprotic CO_2 Electrochemical Reduction. *Adv. Mater.* **35**, 2210658 (2023).
27. Zheng, R. et al. Stable 2e−/2CO_2 Electrochemistry Triggered by Enriched Interfacial Oxygen Mo_2N@$Ti_3C_2O_2$ Elcetrocatalyst for High Rates and High Energy Efficiency Li-CO_2 Batteries. *Adv. Funct. Mater.* **35**, 2412999 (2025).
28. Lu, B. et al. Steering the Orbital Hybridization to Boost the Redox Kinetics for Efficient Li–CO_2 Batteries. *J. Am. Chem. Soc.* **146**, 20814–20822 (2024).
29. Cao, D., Tan, C. & Chen, Y. Oxidative decomposition mechanisms of lithium carbonate on carbon substrates in lithium battery chemistries. *Nat. Commun.* **13**, 4908 (2022).
30. Yang, S., He, P. & Zhou, H. Exploring the electrochemical reaction mechanism of carbonate oxidation in Li–air/CO_2 battery through tracing missing oxygen. *Energy Environ. Sci.* **9**, 1650–1654 (2016).
31. Liu, L. et al. d-Electrons of Platinum Alloy Steering CO Pathway for Low-Charge Potential Li-CO_2 Batteries. *Angew. Chem. Int. Ed.* **64**, e202415728 (2025).
32. Yang, C., Guo, K., Yuan, D., Cheng, J. & Wang, B. Unraveling Reaction Mechanisms of Mo_2C as Cathode Catalyst in a Li-CO_2 Battery. *J. Am. Chem. Soc.* **142**, 6983–6990 (2020).
33. Li, X. et al. Interlayer Expanded MXene Film Cathodes with Rich Defects for Flexible 2-Electron Oxalate-Based Li–CO_2 Batteries: A New Path to Enhanced Energy Efficiency and Durability. *Adv. Mater.* **37**, 2500064 (2025).
34. Zhang, Z. et al. Enhanced Electrochemical Performance of Aprotic Li-CO_2 Batteries with a Ruthenium-Complex-Based

Mobile Catalyst. *Angew. Chem. Int. Ed.* **60**, 16404–16408 (2021).
35. Qi, G., Zhang, J., Chen, L., Wang, B. & Cheng, J. Binder-Free MoN Nanofibers Catalysts for Flexible 2-Electron Oxalate-Based Li-CO_2 Batteries with High Energy Efficiency. *Adv. Funct. Mater.* **32**, 2112501 (2022).
36. Sun, X. et al. Binuclear Cu complex catalysis enabling Li–CO_2 battery with a high discharge voltage above 3.0 V. *Nat. Commun.* **14**, 536 (2023).
37. Li, W. et al. Boosting a practical Li-CO_2 battery through dimerization reaction based on solid redox mediator. *Nat. Commun.* **15**, 803 (2024).
38. Zhou, H. Kinetics of redox-mediated catalysis in batteries. *Nat Catal* **5**, 173–174 (2022).
39. Cao, D. et al. Threshold potentials for fast kinetics during mediated redox catalysis of insulators in Li–O_2 and Li–S batteries. *Nat Catal* **5**, 193–201 (2022).
40. Zhang, Y., Zhang, X., Jiao, L., Meng, Z. & Jiang, H.-L. Conductive Covalent Organic Frameworks of Polymetallophthalocyanines as a Tunable Platform for Electrocatalysis. *J. Am. Chem. Soc.* **145**, 24230–24239 (2023).
41. Li, L. et al. Longitudinally Grafting of Graphene with Iron Phthalocyanine-based Porous Organic Polymer to Boost Oxygen Electroreduction. *Angew. Chem. Int. Ed.* **62**, e202301642 (2023).
42. Hammer, B., Hansen, L. B. & Nørskov, J. K. Improved adsorption energetics within density-functional theory using revised Perdew-Burke-Ernzerhof functionals. *Phys. Rev. B.* **59**, 7413–7421 (1999).
43. Kresse, G. & Furthmüller, J. Efficient iterative schemes for ab initio total-energy calculations using a plane-wave basis set. *Phys. Rev. B.* **54**, 11169–11186 (1996).
44. Perdew, J. P., Burke, K. & Ernzerhof, M. Generalized Gradient Approximation Made Simple. *Phys. Rev. Lett.* **77**, 3865–3868 (1996).
45. Nørskov, J. K. et al. Origin of the Overpotential for Oxygen Reduction at a Fuel-Cell Cathode. *J. Phys. Chem. B* **108**, 17886–17892 (2004).

Acknowledgements

This work was supported by the National Natural Science Foundation of China (No. 52471237) and the Young Talent Support Plan of Xi'an Jiaotong University (for X. F. H.). The authors deeply acknowledge Mr. Chang Huang, Mrs. Jia Liu, Mr. Zijun Ren and Mrs. Yan Liang at the Instrument Analysis Center of Xi'an Jiaotong University for assistance with in-situ XRD, in-situ Raman, SEM and TOF-SIMS, respectively.

Author Contributions

Ning Zhao and Yi Zhang have contributed equally to this work. All authors have given approval to the final version of the Manuscript.

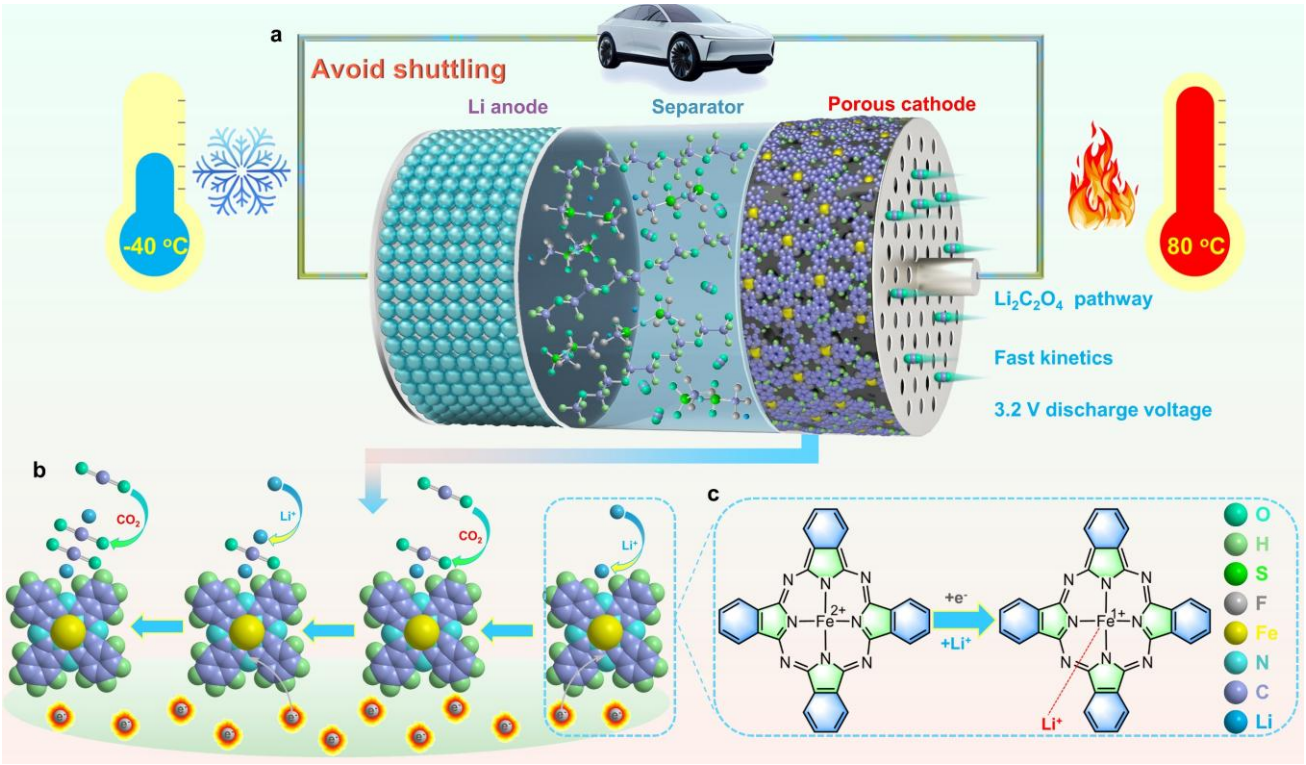
Competing interests

The authors declare no competing interests.

Additional information

Supporting information The Supporting Information is available free of charge on the Nature Communications website.

Correspondence and requests for materials should be addressed to Xiaofei Hu or Zheng Meng.



Scheme 1. a) The Model of Li-CO_2 battery with pFe^{II}Pc as solid-phase redox mediator. b) Soild-phase pFe^{II}Pc-mediated reaction mechanism towards $Li_2C_2O_4$ route. c) The process of pFe^{II}Pc gaining electrons and adsorbing Li^+.

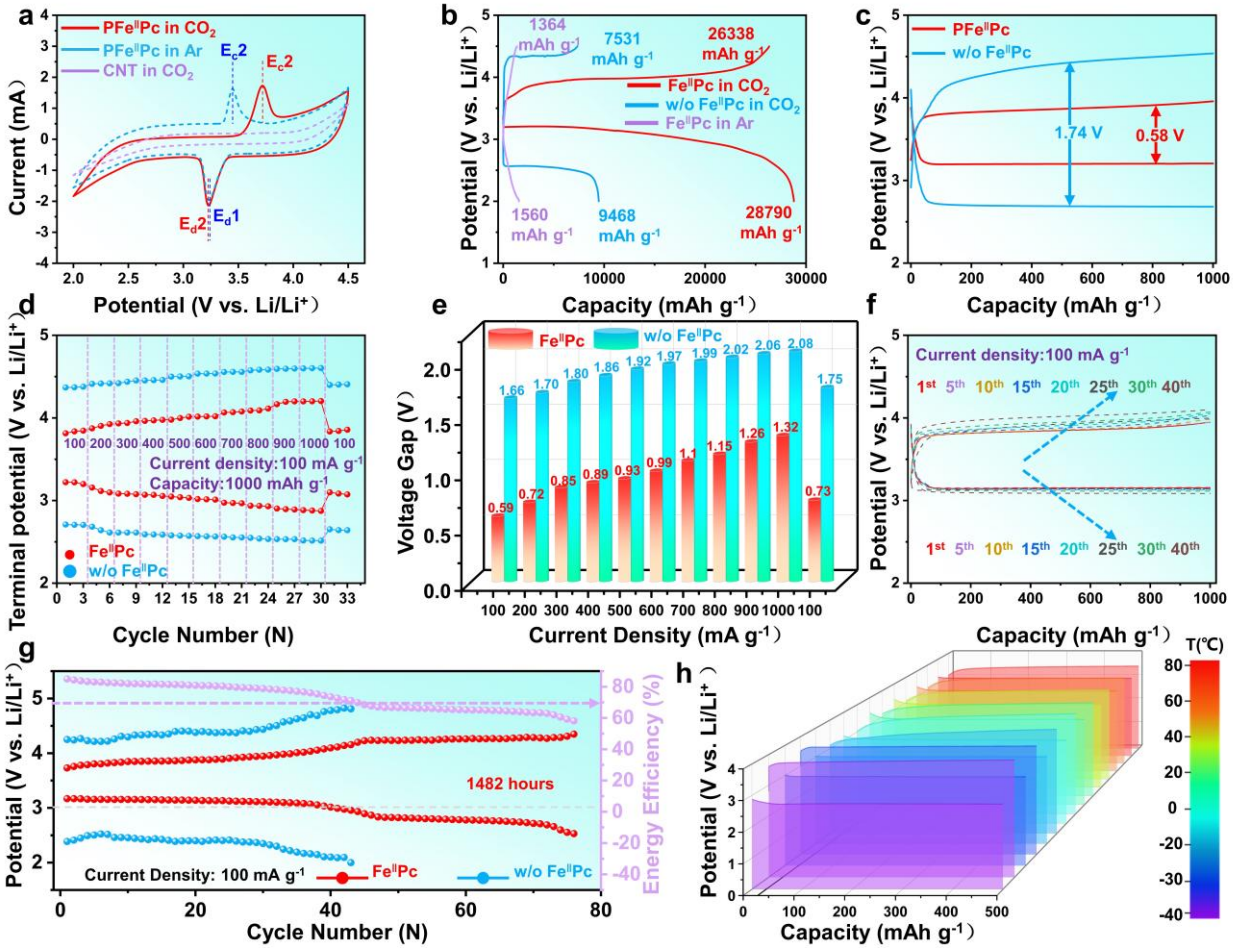


Figure 1. a) The CV plots of CNTs and pFe^{II}Pc cathode in Ar and CO_2 atmosphere. b) Full deep discharge/charge profiles of CNTs and solid pFe^{II}Pc cathode under Ar and CO_2 at a current density of 100 mA g^{-1}. c) Comparison of the galvanostatic charge-discharge profiles of Li-CO_2 batteries with pFe^{II}Pc and without pFe^{II}Pc within the cut-off capacity of 1000 mAh g^{-1}. d) Rate performance of Li-CO_2 batteries with and without pFe^{II}Pc. e) Potential gap comparison between pFe^{II}Pc and CNT cathode at different current densities. f) Recyclability of Li-CO_2 battery with pFe^{II}Pc with a cut-off capacity of 1000 mAh g^{-1} at 100 mA g^{-1}. g) Median discharge/charge voltage plateau voltages for pFe^{II}Pc and CNT electrode at 100 mA g^{-1}, with the inset purple dots referring to energy efficiency. h) Charge−discharge profiles of Li-CO_2 battery with pFe^{II}Pc as solid-state redox mediators across a wide temperature range with a cut-off capacity of 500 mAh g^{-1} at 20 mA g^{-1}.

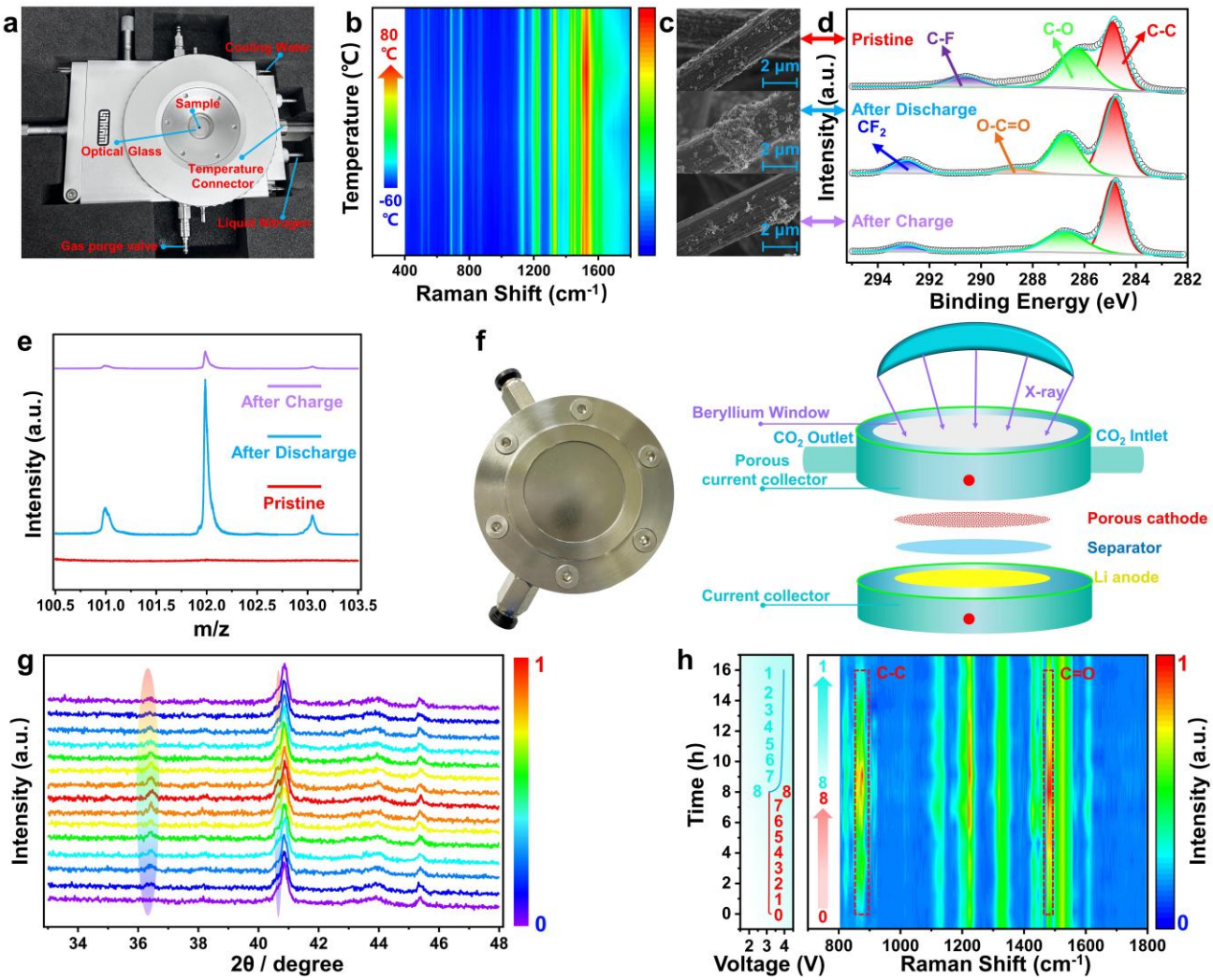


Figure 2. a) Optical image of the variable-temperature in-situ Raman device. b) In-situ Raman spectra of pFe^{II}Pc measured at different temperatures. c) SEM of Li-CO_2 batteries with pFe^{II}Pc as solid-state redox mediators at pristine, discharged and recharged, respectively. d) The C 1s XPS spectra Li-CO_2 batteries with pFe^{II}Pc as solid-state redox mediators at pristine, discharged and recharged states. e) m/z of 100.5-103.5. f) The structure of in-situ Li-CO_2 XRD battery. g) In-situ XRD patterns of Li-CO_2 batteries with pFe^{II}Pc at 200 mA g^{-1}. h) Charge-discharge profiles of Li-CO_2 batteries with pFe^{II}Pc at 200 mA g^{-1} with 16 selected states and the corresponding in-situ Raman spectra.

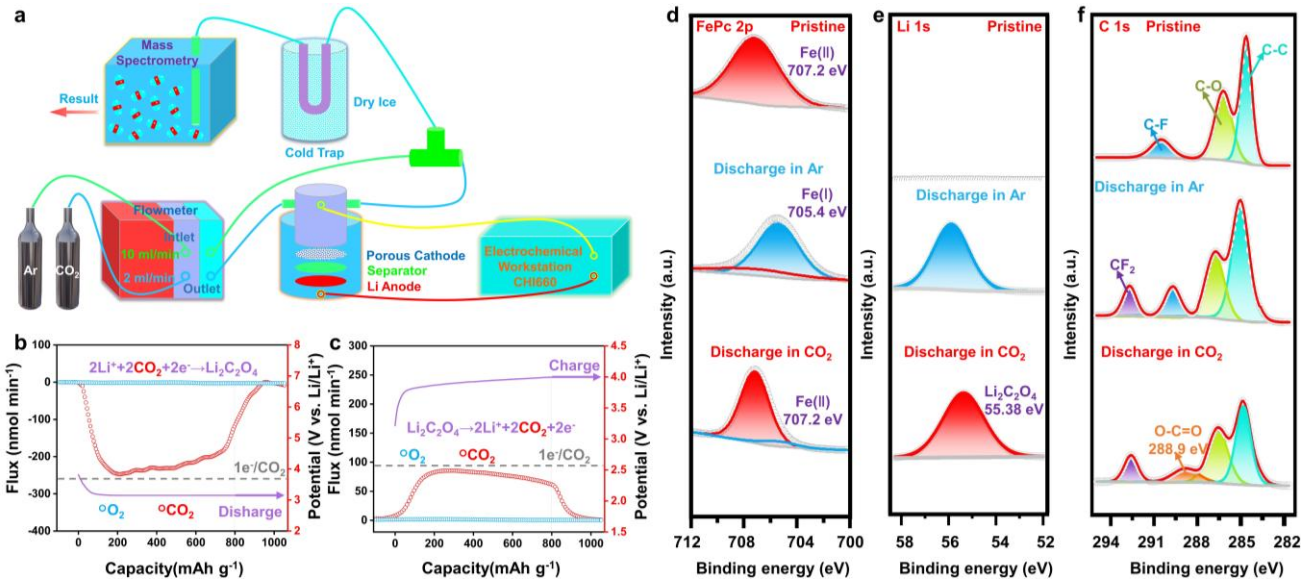


Figure 3. a) Schematic diagram of the in-situ DEMS for the discharge process of the Li-CO_2 battery. In-situ DEMS profiles of Li-CO_2 batteries with $pFe^{II}Pc$ as solid-state redox mediators at 150 μA after b) discharge process c) charge process. d) XPS $pFe^{II}Pc$ 2p spectra, e) Li 1s and f) C 1s of solid-phase $pFe^{II}Pc$ cathode at different atmospheres and discharge stages.

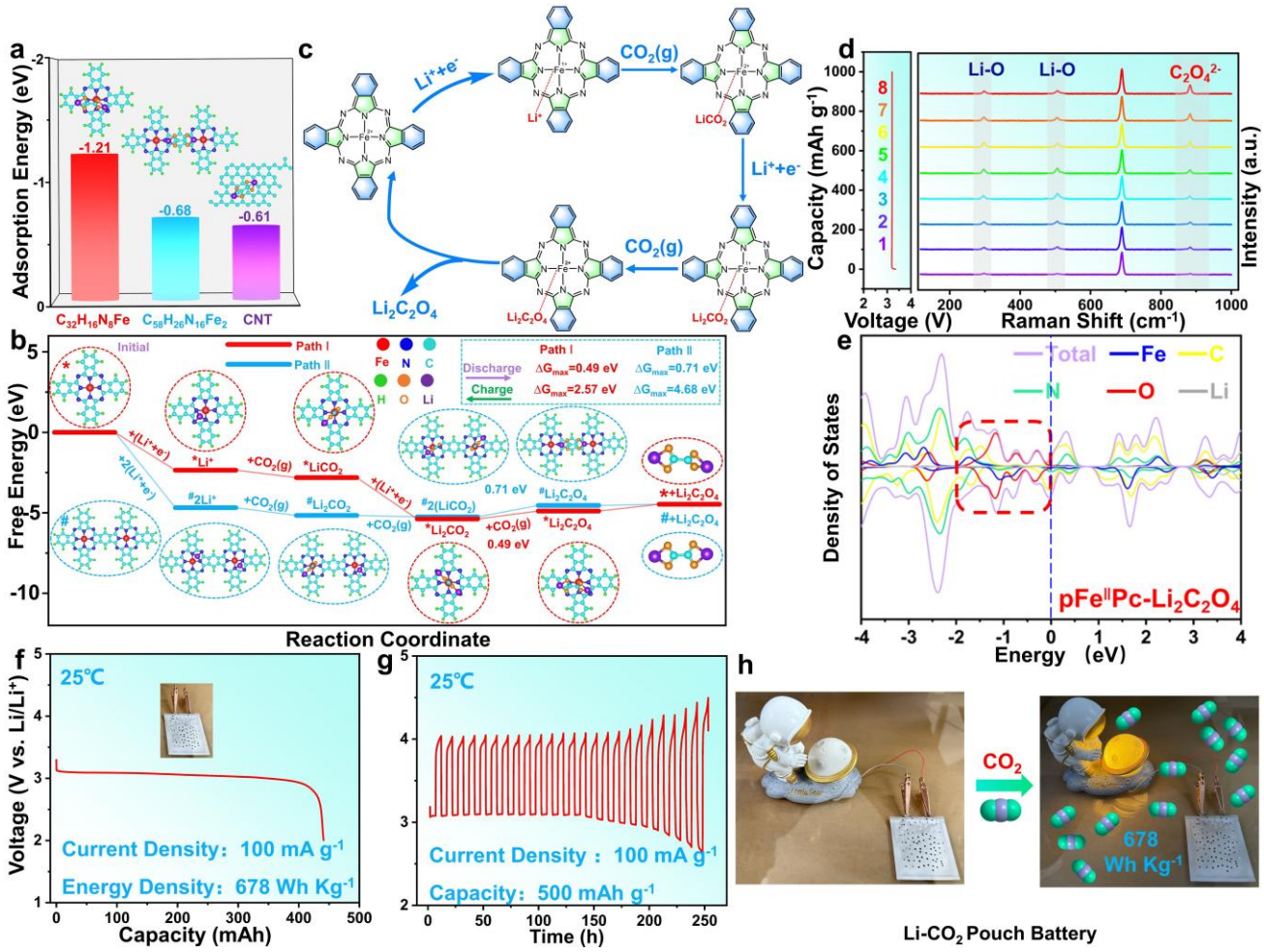
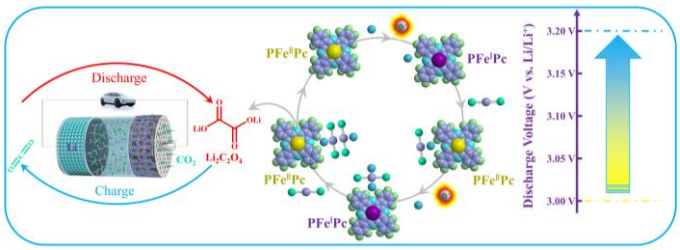


Figure 4. a) Optimized structure and adsorption energy of $Li_2C_2O_4$ on $C_{32}H_{16}N_8Fe$, $C_{58}H_{26}N_{16}Fe_2$, and CNT. b) Free energy diagrams of different nucleation pathways of $Li_2C_2O_4$ on $C_{32}H_{16}N_8Fe$ and $C_{58}H_{26}N_{16}Fe_2$. c) Proposed mechanism of $pFe^{II}Pc$ as solid-state redox mediators mediated CO_2 reduction process in Li-CO_2 battery. d) Discharge profiles of Li-CO_2 batteries with $pFe^{II}Pc$ with 8 selected states and the corresponding in-situ Raman spectra. e) Fermi level of the $C_{32}H_{16}N_8Fe$ after $Li_2C_2O_4$ adsorption. f) Full discharge capacity of a Li-CO_2 pouch cell fabricated with $pFe^{II}Pc$ cathode. g) Cycling performance of a Li-CO_2 pouch cell at room temperature. h) The Li-CO_2 pouch cell with $pFe^{II}Pc$ lights up the LED of the astronaut model.

Entry for the Table of Contents



The $Li_2C_2O_4$-product pathway Li-CO_2 battery with $pFe^{II}Pc$ as solid-state redox mediator exhibits prominent temperature adaptability (-40~80 °C), high electrochemical stability (1482 hours), and especially a higher discharge voltage of 3.2 V than the theoretical value (3.01 V). The pouch cell achieves an energy density of 678 Wh kg^{-1}. During discharge, $pFe^{I}Pc$ preferentially accepts electrons from the anode instead of CO_2, being reduced to $pFe^{I}Pc$. Subsequently, $pFe^{I}Pc$ rapidly transfers these electrons to CO_2 (thereby being oxidized back to $pFe^{II}Pc$), and ultimately the reduced CO_2 reacts with Li^+ to form $Li_2C_2O_4$.

Supplementary Files

This is a list of supplementary files associated with this preprint. Click to download.

- SupportingInformation.docx